

Large-scale power spectrum and structures from the ENEAR galaxy peculiar velocity catalogue

S. Zaroubi,^{1★} M. Bernardi,^{1,2} L. N. da Costa,^{3,4} Y. Hoffman,⁵ M. V. Alonso,⁶ G. Wegner,⁷
C. N. A. Willmer^{4,8} and P. S. Pellegrini⁴

¹Max Planck Institut für Astrophysik, Karl-Schwarzschild-Str. 1, 85741 Garching, Germany

²The University of Chicago, 5640 South Ellis Avenue, Chicago, IL 60637, USA

³European Southern Observatory, Karl-Schwarzschild-Str. 2, 85748 Garching, Germany

⁴Observatório Nacional, Rua General Jose Cristino 77, Rio de Janeiro, RJ 20921, Brazil

⁵Racah Institute of Physics, The Hebrew University, Jerusalem 91904, Israel

⁶Observatorio Astronómico de Córdoba Laprida 854, Córdoba (5000), Argentina

⁷Department of Physics and Astronomy, 6127 Wilder Laboratory, Dartmouth College, Hanover, NH 03755-3528, USA

⁸UCO/Lick Observatory, University of California, 1156 High Street, Santa Cruz, CA 95064, USA

Accepted 2001 April 20. Received 2001 March 28; in original form 2000 June 1

ABSTRACT

We estimate the *mass* density fluctuations power spectrum (PS) on large scales by applying a maximum likelihood technique to the peculiar velocity data of the recently completed redshift–distance survey of early-type galaxies (hereafter ENEAR). Parametric cold dark matter (CDM)-like models for the PS are assumed, and the best-fitting parameters are determined by maximizing the probability of the model given the measured peculiar velocities of the galaxies, their distances and estimated errors. The method has been applied to CDM models with and without *COBE* normalization. The general results are in agreement with the high-amplitude power spectra found from similar analyses of other independent all-sky catalogue of peculiar velocity data such as MARK III and SFI, in spite of the differences in the way these samples were selected, the fact that they probe different regions of space and galaxy distances are computed using different distance relations. For example, at $k = 0.1 h \text{ Mpc}^{-1}$ the power spectrum value is $P(k)\Omega^{1.2} = (6.5 \pm 3) \times 10^3 (h^{-1} \text{ Mpc})^3$ and $\eta_8 \equiv \sigma_8 \Omega^{0.6} = 1.1^{+0.2}_{-0.35}$; the quoted uncertainties refer to 3σ error level. We also find that, for Λ CDM and OCDM *COBE*-normalized models, the best-fitting parameters are confined by a contour approximately defined by $\Omega h^{1.3} = 0.377 \pm 0.08$ and $\Omega h^{0.88} = 0.517 \pm 0.083$ respectively. Γ -shape models, free of *COBE* normalization, result in the weak constraint of $\Gamma \geq 0.17$ and in the rather stringent constraint of $\eta_8 = 1.0 \pm 0.25$. All quoted uncertainties refer to 3σ confidence level (c.l.).

The calculated PS has been used as a prior for Wiener reconstruction of the density field at different resolutions and the three-dimensional velocity field within a volume of radius $\approx 80 h^{-1} \text{ Mpc}$. All major structures in the nearby Universe are recovered and are well matched to those predicted from all-sky redshift surveys. The robustness of these features has been tested with constrained realizations (CR). Analysis of the reconstructed three-dimensional velocity field yields a small bulk-flow amplitude ($\sim 160 \pm 60 \text{ km s}^{-1}$ at $60 h^{-1} \text{ Mpc}$) and a very small rms value of the tidal field ($\sim 60 \text{ km s}^{-1}$). The results give further support to the picture that most of the motion of the Local Group arises from mass fluctuations within the volume considered.

Key words: methods: statistical – galaxies: distances and redshifts – cosmology: observations – cosmology: theory – dark matter – large-scale structure of Universe.

★E-mail: saleem@mpa-garching.mpg.de

1 INTRODUCTION

The canonical model of cosmology assumes that large-scale structure has grown out of small density perturbations via the process of gravitational instability. These initial fluctuations are usually assumed to satisfy the statistics of a Gaussian random field, solely characterized by its power spectrum (PS). In the linear regime, the fluctuations grow self-similarly and retain their initial distribution and power spectrum shape. Therefore, mapping the underlying cosmological velocity field and its power spectrum on large scales provides a direct probe of the origin of structure in the Universe.

The PS, the three-dimensional distribution of luminous matter and the predicted peculiar velocity field have been derived from a variety of data sets, especially from all-sky redshift surveys (see e.g. Strauss & Willick 1995 for a review of earlier work; Sutherland et al. 1999; Branchini et al. 1999). Unfortunately, however, the distribution of galaxies in these catalogues is not necessarily an unbiased tracer of the underlying mass distribution, and suffers from the infamous ‘galaxy biasing’ problem. Furthermore, in estimates from redshift surveys, uncertainties arise from the complicated relation between the real-space and the redshift-space distributions, known as redshift distortions (e.g. Kaiser 1987; Zaroubi & Hoffman 1996). In order to avoid these problems altogether it is advantageous to appeal to dynamical data, in particular catalogues of galaxy peculiar velocities on large scales.

Peculiar velocities enable a direct and reliable determination of the mass PS and distribution, under the natural assumption that the galaxies are unbiased tracers of the large-scale, gravitationally induced, velocity field. Furthermore, because peculiar velocities are non-local and have contributions from different scales, analysis of the peculiar velocity field provides information on scales somewhat larger than the sampled region (e.g. Hoffman et al. 2001). For the same reason peculiar velocities are adequately described by linear theory even when densities become quasi-linear (e.g. Freudling et al. 1999). Consequently, the dynamics and the distribution of peculiar velocities are well described by the linear regime of gravitational instability and by a Gaussian probability distribution function (PDF).

Assuming that both the underlying velocity field and the errors are drawn from independent random Gaussian fields, the observed peculiar velocities constitute a multivariate Gaussian data set, albeit with sparse and inhomogeneous sampling. The corresponding *posterior* PDF is a multivariate Gaussian that is completely determined by the assumed PS and covariance matrix of errors. Under these conditions one can write the joint PDF of the model PS and the underlying velocity or density field.

The purpose of the present study is to calculate, from the joint PDF, the PS and 3D mass distribution, as well as the 3D peculiar velocity field, as derived from the newly completed ENEAR galaxy peculiar velocity catalogue (da Costa et al. 2000a, hereafter Paper I). This is facilitated by the following two steps.

First, the PS model parameters are estimated by maximizing the likelihood function given the model (Zaroubi et al. 1997). An identical likelihood estimation of the power spectrum has been previously applied to the Mark III (Zaroubi et al. 1997) and the SFI (Freudling et al. 1999) data sets. In both cases the analysis yielded a high-amplitude power spectrum. Although the results from those two catalogues are consistent with each other, they are marginally inconsistent with the power spectra measured from redshift catalogues (e.g. da Costa et al. 1996; Sutherland et al. 1999),

inferred from the analysis of the velocity correlation function (e.g. Borgani et al. 2000a,b), and from velocity–velocity comparisons (e.g. Davis, Nusser & Willick 1996; da Costa et al. 1998). One of our goals is to apply the same methodology to the new ENEAR catalogue that was used with the Mark III and SFI. This should directly test the reproducibility of the results with an independent sample based on a different distance indicator but probing a comparable volume.

Secondly, the Wiener filter (WF) solution of the field is recovered by finding the most probable field given the PS and the data (Zaroubi et al. 1995; Zaroubi, Hoffman & Dekel 1999). Constrained realizations (CR) are then used to sample the statistical scatter around the WF field (Hoffman & Ribak 1991). The mass density PS is used to calculate the smoothed Wiener filtered density and 3D velocity fields given the measured radial velocities (Zaroubi et al. 1995, 1999) – for other applications of the WF in cosmology see for example Bunn et al. (1994), Fisher et al. (1995) and Lahav et al. (1994). The WF provides an optimal estimator of the underlying field in the sense of a minimum-variance solution given the data and an assumed *prior* model (Wiener 1949; Press et al. 1992). The *prior* defines the data autocorrelation and the data–model cross-correlation matrices. In the case where the data are drawn from a random Gaussian field, the WF estimator coincides with the conditional mean field and with the most probable configuration given the data (see Zaroubi et al. 1995). It should be noted that Kaiser & Stebbins (1991) were the first to propose a Bayesian solution to the problem of reconstruction from peculiar velocity data sets. Finally, the recovered three-dimensional velocity field is used to compute the amplitude of the bulk flow and to decompose the velocity field in terms of divergent and tidal components, which enables one to separate the contribution to the measured peculiar velocity field from mass fluctuations within and outside the volume probed by the data (Hoffman et al. 2001).

The methods adopted in this study do not involve any explicit window function, weighting or smoothing of the data. In addition, they automatically underweight noisy, unreliable data. However, a few simplifying assumptions are required: (1) peculiar velocities are drawn from a Gaussian random field; (2) peculiar velocities are related to the densities through linear theory; (3) errors in the D_n – σ inferred distances constitute a Gaussian random field with two components, the first scales linearly with distance while the second models the non-linear evolution of the velocities as a constant scatter. It should be noted that the distance indicator usually gives a log-normal scatter, however, Zaroubi et al. (1997) and Freudling et al. (1999) have shown that using a Gaussian distribution gives a satisfactory approximation. The need to assume a parametric functional form for the PS is also a limitation.

The outline of this paper is as follows. In Section 2 we briefly describe the peculiar velocity data used in the present analysis. The PS analysis is carried out in Section 3. The Wiener filtering is applied to the ENEAR data in Section 4, where maps of the density field are presented and compared with those predicted from redshift surveys. Also shown in this section are the recovered three-dimensional velocity field and the results of its analysis. Our results are summarized and discussed in Section 5.

2 THE DATA

In the present analysis, we use the ENEAR redshift–distance survey described in greater detail in Paper I of this series. Briefly, the ENEAR sample consists of roughly 1600 early-type galaxies

brighter than $m_B = 14.5$ and with $cz \leq 7000 \text{ km s}^{-1}$, for which $D_n - \sigma$ distances are available for 1359 galaxies. Of these 1145 were deemed suitable for peculiar velocity analysis according to well-defined criteria (Paper I). To the magnitude-limited sample we added 285 fainter and/or with redshifts $> 7000 \text{ km s}^{-1}$, 129 within the same volume as the magnitude-limited sample. The sample of galaxies within 7000 km s^{-1} thus consists of 1274 galaxies assigned to 696 objects – 282 groups/clusters and 414 individual galaxies.

The cluster sample consists of 569 galaxies in 28 clusters, which are used to derive the distance relation. Over 80 per cent of the galaxies in the magnitude-limited sample and roughly 60 per cent of the cluster galaxies have new spectroscopic and R -band photometric data obtained as part of this programme. Furthermore, repeated observations of several galaxies in the sample provide overlaps between observations conducted with different telescope/instrument configurations and with data available from other authors. These overlaps tie all measurements into a common system, thereby ensuring the homogeneity of the entire data set. In contrast to other samples, new observations conducted by the same group are available over the entire sky. The comparison between the sample of galaxies with distances and the parent catalogue also shows that the sampling across the sky is uniform.

Individual galaxy distances were estimated from a direct $D_n - \sigma$ template relation derived by combining all the available cluster data (Bernardi et al., in preparation), corrected for incompleteness and associated diameter bias (Lynden-Bell et al. 1988). From the observed scatter of the template relation the estimated fractional error in the inferred distance of a galaxy is $\Delta \sim 0.19$, nearly independent of the velocity dispersion.

As early-type galaxies are found preferentially in high-density regions, galaxies have been assigned to groups/clusters using well-defined criteria imposed on their projected separation and velocity difference relative to the centre of groups and clusters. These systems were identified using objective algorithms applied to the available magnitude-limited samples, comprising all morphological types, with complete redshift information probing the same volume. For membership assignment we used group catalogues published by Geller & Huchra (1983), Maia, da Costa & Latham (1989) and Ramella, Pisani & Geller (1997) as well as unpublished results covering other regions of the sky. The characteristic size and velocity dispersion of these groups/clusters was used to establish the membership of the ENEAR early-types, as described in Paper I. We find isolated galaxies, groups with only one early-type, and groups with two or more early-types. Early-type galaxies in a group/cluster are replaced by a single object having the following properties.

- (1) The redshift given by the group's mean redshift, which is determined considering all morphologies. We have compared these redshifts with those obtained using only early-types. We find that the difference is insignificant, showing an offset in the mean of $\leq 20 \text{ km s}^{-1}$ and a scatter of $\sim 100 \text{ km s}^{-1}$.
- (2) The distance given by the error-weighted mean of the inferred distances, for groups with two or more early-types.
- (3) The fractional distance error given by Δ/\sqrt{N} , where N is the number of early-types in the group.

In some cases groups were identified with Abell/ACO clusters within the same volume as the ENEAR sample and fainter cluster galaxies were added, as described in Paper I. In

the analysis below we compute the dipole component of the velocity field out to 6000 km s^{-1} as probed by all objects, and by splitting the sample into two independent subsamples consisting of field galaxies and groups/clusters. The latter is done to evaluate the amplitude of possible sampling errors directly from the data.

The inferred distances are corrected for the homogeneous and inhomogeneous Malmquist bias (IMB). The latter was estimated using the PCSz density field (Branchini et al. 1999), corrected for the effects of peculiar velocities, in the expressions given by Willick et al. (1997). In this calculation we also include the correction for the redshift limit of the sample. A complete account of the sample used and the corrections applied will be presented in a subsequent paper of this series.

3 POWER SPECTRUM

The calculation of the matter PS from the peculiar velocity data by means of likelihood analysis requires a relation between the velocity correlation function and the power spectrum. Define the two-point velocity correlation (3×3) tensor as the average over all pairs of points \mathbf{r}_i and \mathbf{r}_j that are separated by $\mathbf{r} = \mathbf{r}_j - \mathbf{r}_i$,

$$\Psi_{\mu\nu}(\mathbf{r}) \equiv \langle v_\mu(\mathbf{r}_i)v_\nu(\mathbf{r}_j) \rangle, \quad (1)$$

where $v_\mu(\mathbf{r}_i)$ is the μ component of the peculiar velocity at \mathbf{r}_i . In linear theory, the velocity correlation tensor can be expressed in terms of two scalar functions of $r = |\mathbf{r}|$ (Górski 1988), computed from the parallel and perpendicular components of the peculiar velocity, relative to the separation vector \mathbf{r} ,

$$\Psi_{\mu\nu}(\mathbf{r}) = \Psi_\perp(r)\delta_{\mu\nu} + [\Psi_\parallel(r) - \Psi_\perp(r)]\hat{r}_\mu\hat{r}_\nu. \quad (2)$$

The spectral representation of these radial correlation functions is

$$\Psi_{\perp,\parallel}(r) = \frac{H_0^2 f^2(\Omega)}{2\pi^2} \int_0^\infty P(k)K_{\perp,\parallel}(kr) dk, \quad (3)$$

where $K_\perp(x) = j_1(x)/x$ and $K_\parallel(x) = j_0 - 2j_1(x)/x$, with $j_l(x)$ the spherical Bessel function of order l . The cosmological Ω dependence enters, as usual in linear theory, via $f(\Omega) \approx \Omega^{0.6}$, and H_0 is the Hubble constant. A parametric functional form of $P(k)$ thus translates to a parametric form of $\Psi_{\mu\nu}$. Note that the quantity that can be derived from peculiar-velocity data via the linear approximation is $f^2(\Omega)P(k)$, where P is the mass density PS.

Let \mathbf{m} be the vector of model parameters and \mathbf{d} the vector of N data points. Then Bayes' theorem states that the *posterior* probability density of a model given the data is

$$\mathcal{P}(\mathbf{m}|\mathbf{d}) = \frac{\mathcal{P}(\mathbf{m})\mathcal{P}(\mathbf{d}|\mathbf{m})}{\mathcal{P}(\mathbf{d})}. \quad (4)$$

The denominator is merely a normalization constant. The probability density of the model parameters, $\mathcal{P}(\mathbf{m})$, is unknown, and in the absence of any other information we assume it is uniform within a certain range. The conditional probability of the data given the model, $\mathcal{P}(\mathbf{d}|\mathbf{m})$, is the likelihood function, $\mathcal{L}(\mathbf{d}|\mathbf{m})$. The objective in this approach, which is to find the set of parameters that maximizes the probability of the model given the data, is thus equivalent to maximizing the likelihood of the data given the model (cf. Jaffe & Kaiser 1995; Zaroubi et al. 1997).

Assuming that the velocities are a Gaussian random field, the two-point velocity correlation tensor Ψ fully characterizes the statistics of the velocity field. Define the radial velocity correlation

$(N \times N)$ matrix U_{ij} by

$$U_{ij} = \hat{\mathbf{r}}_i \cdot \Psi \hat{\mathbf{r}}_j = \Psi_{\perp}(r) \sin \theta_i \sin \theta_j + \Psi_{\parallel}(r) \cos \theta_i \cos \theta_j, \quad (5)$$

where i and j refer to the data points, $r = |\mathbf{r}| = |\mathbf{r}_j - \mathbf{r}_i|$ and the angles are defined by $\cos \theta_i = \hat{\mathbf{r}}_i \cdot \hat{\mathbf{r}}$ (Górski 1988; Groth, Juszkiewicz & Ostriker 1989). Let the inferred radial peculiar velocity at \mathbf{r}_i be u_i^o , with the corresponding error ϵ_i also assumed to be a Gaussian random variable. The observed correlation matrix is then $\tilde{U}_{ij} = U_{ij} + \epsilon_i^2 \delta_{ij}$, and the likelihood of the N data points is

$$\mathcal{L} = [(2\pi)^N \det(\tilde{U}_{ij})]^{-1/2} \exp\left(-\frac{1}{2} \sum_{ij} u_i^o \tilde{U}_{ij}^{-1} u_j^o\right). \quad (6)$$

Given that the correlation matrix, \tilde{U}_{ij} , is symmetric and positive definite, we can use the Cholesky decomposition method (Press et al. 1992) for computing the likelihood function (equation 6). The significant contribution of the errors to the diagonal terms makes the matrix especially well-conditioned for decomposition.

The errors are assumed to have two contributions: the first is the usual D_n - σ distance proportional errors (about 19 per cent per galaxy for ENEAR). The second is a constant error that accounts for the non-linear velocities of galaxies in the high-density environment in which early-type galaxies reside. This term represents our poor understanding of the complex correlations introduced by non-linear evolution. For each power spectrum model, we have performed the likelihood analysis assuming this constant value to be either null or 250 km s^{-1} but, as shown below, the difference in the results are only marginal and do not affect our general conclusions.

The Bayesian analysis measures only the relative likelihood of different models. An absolute measure of goodness of fit is provided by the χ^2 per degree of freedom (hereafter d.o.f.), which we use as a check of the best parameters obtained by the likelihood analysis. The χ^2 is simply defined as $\sum_{ij} u_i^o \tilde{U}_{ij}^{-1} u_j^o$, which appears in the exponent of equation (6).

3.1 COBE-normalized CDM models

We first restrict our attention to the generalized family of CDM cosmological models, allowing variations in the cosmological parameters Ω , Λ and h . Furthermore, four-year COBE normalization is imposed as an additional external constraint. The general form of the PS for these models is

$$P(k) = A_{\text{COBE}}(n, \Omega, \Lambda) T^2(\Omega, \Omega_b, h; k) k^n, \quad (7)$$

where the CDM transfer function proposed by Sugiyama (1995) is adopted,

$$T(k) = \frac{\ln(1 + 2.34q)}{2.34q} \times [1 + 3.89q + (16.1q)^2 + (5.46q)^3 + (6.71q)^4]^{-1/4}, \quad (8)$$

$$q = k[\Omega h \exp(-\Omega_b - h_{50}^{1/2} \Omega_b / \Omega) h \text{ Mpc}^{-1}]^{-1}. \quad (9)$$

The parameters Ω and h are varied such that they span the range of currently popular CDM models, including Λ CDM ($\Omega + \Lambda = 1$, $\Omega \leq 1$) and OCDM ($\Lambda = 0$, $\Omega \leq 1$). In all cases, the baryonic density is assumed to be $\Omega_b = 0.019 h^{-2}$, which is the value currently favoured by primordial nucleosynthesis analysis (e.g. Burles & Tytler 1998). We limit our investigation to models without tilt, namely to those with $n = 1$. For each model, the

normalization of the PS is fixed by the COBE 4-yr data (Bennett et al. 1996). In fact, this is the only difference between the OCDM and Λ CDM power spectra in our calculation; for more details see Zaroubi et al. (1997 and references therein).

Fig. 1(a) shows the likelihood contour map in the Ω - h plane, for the Λ CDM family of models with $n = 1$ using Sugiyama's (1995) mass power spectrum fit to the COBE 4-year data. In this case, the error matrix includes the 250 km s^{-1} contribution mentioned earlier to model the non-linear evolution of the galaxies. The most probable parameters in this case (in the range $\Omega \leq 1$) are $\Omega = 1$ and $h = 0.5$. The elongated contours clearly indicate that neither Ω nor h are independently well constrained. The combination of these two parameters is rather degenerate. What is being determined is

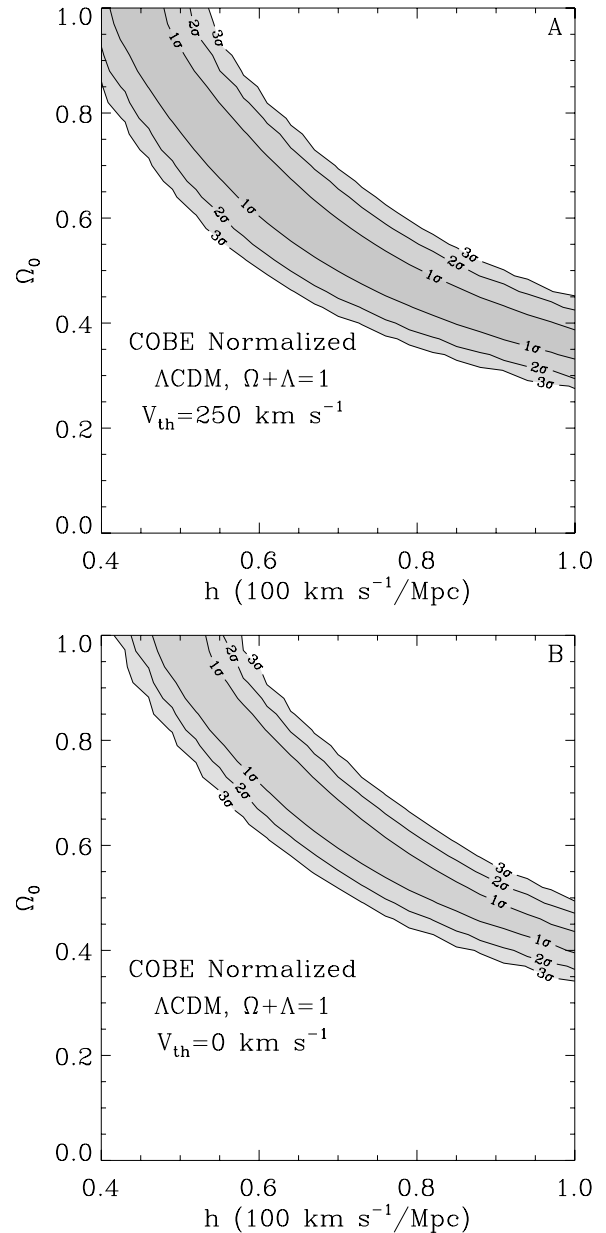


Figure 1. Contour map of \ln likelihood in the h - Ω plane for Λ CDM models with 250 km s^{-1} thermal error component (upper panel) and zero thermal error (lower panel). The contours denote the most likely values within 1, 2 and 3σ c.l.

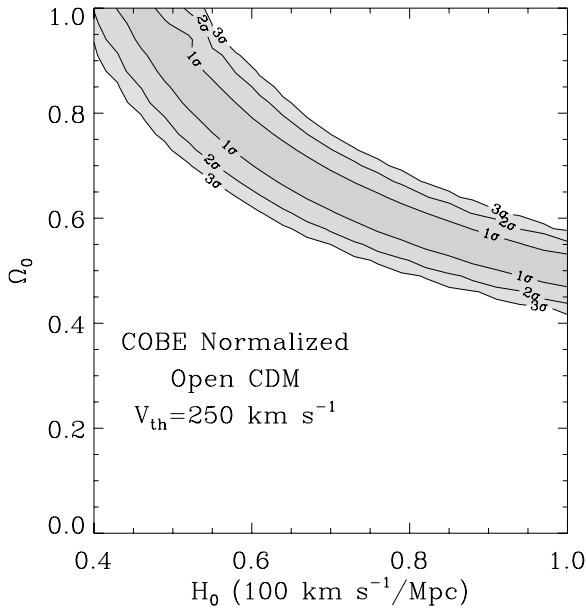


Figure 2. Same as Fig. 1(a) but for OCDM models.

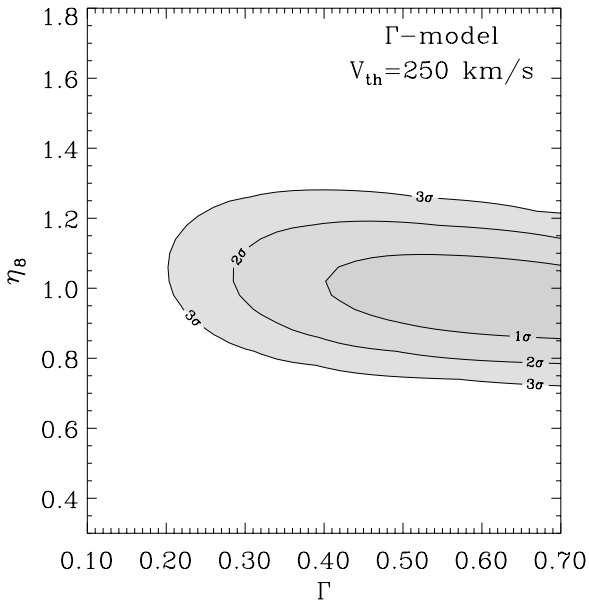


Figure 3. Contour map of \ln likelihood for the Γ model in the Γ - η_8 plane. The contours denote the 1, 2 and 3σ c.l.

Ωh^x with $x \sim 1$ and this is tightly constrained by the elongated ridge of high likelihood.

Fig. 1(b) shows the likelihood results for the same Λ CDM model shown in Fig. 1(a) but with no random contribution to the error matrix. The contours in Fig. 1(b) show very little changes relative to those shown in panel (a), notably they get tighter and the best values of Ω for a given Hubble constant are somewhat higher. The addition of a reasonable random component to the error matrix does not alter the results in any significant way for any of the PS models considered in this study. For the rest of the PS models we show the calculation with the addition of a constant error of 250 km s^{-1} .

Fig. 2 shows the similar likelihood map for OCDM with $n = 1$. The most probable values here are $\Omega = 0.53$ and $h = 1$.

The values of Ω and h are not independently constrained here as well.

We can thus quote stringent constraints on the conditional best value of h given Ω for the COBE-normalized CDM models shown in Figs 1(a) and 2: $\Omega \approx (0.377 \pm 0.08) h^{-1.3}$ for Λ CDM, and $\Omega \approx (0.517 \pm 0.083) h^{-0.88}$ for OCDM.

3.2 The Γ model

To recover the PS from the velocity data independent of the COBE normalization, we use as a parametric prior the so-called Γ model (e.g. Efstathiou, Bond & White 1992),

$$P(k) = AkT^2(k),$$

$$T(k) = \{1 + [ak/\Gamma + (bk/\Gamma)^{3/2} + (ck/\Gamma)^2]^\nu\}^{-1/\nu}, \quad (10)$$

with $a = 6.4 h^{-1} \text{ Mpc}$, $b = 3.0 h^{-1} \text{ Mpc}$, $c = 1.7 h^{-1} \text{ Mpc}$ and $\nu = 1.13$. The free parameters to be determined by the likelihood analysis are the normalization factor $\eta_8 \equiv \sigma_8 \Omega^{0.6}$ and the Γ parameter. In the context of the CDM cosmological model, Γ has a specific cosmological interpretation, $\Gamma = \Omega h$. Here, however, equation (10) serves as a generic function with logarithmic slopes $n = 1$ and -3 on large and small scales respectively, and with a turnover at some intermediate wavenumber that is determined by the single shape parameter Γ .

Fig. 3 shows the contour map of $\ln \mathcal{L}$ in the Γ - η_8 plane. Although the likelihood analysis in poses a strong constraint on the allowed values of η_8 ($= 1.0^{+0.3}_{-0.28}$ with 3σ c.l.), it only weakly constrains the value of Γ (≥ 0.18 at the 3σ c.l.), and $\Gamma = 0.25$ is excluded at the 2σ c.l..

3.3 Results and comparison between the various models

The best fit models for each CDM family have a comparable likelihood, with the most likely model being the OCDM model with $\Omega = 0.53$ and $h = 1$. All best-fitting models agree within ≈ 20 per cent for $k > 0.1 h \text{ Mpc}^{-1}$. The amplitude of the PS at $k = 0.1 h \text{ Mpc}^{-1}$ for all models lies within $P(k)\Omega^{1.2} = (6.5 \pm 3) \times 10^3 (h^{-1} \text{ Mpc})^3$ and the values of η_8 are within the range $1.1^{+0.2}_{-0.35}$.

Fig. 4 shows the power spectrum of the most likely COBE-normalized model and the 3σ errors about it. It also shows the PS corresponding to the most likely Λ CDM and Γ models. Within the errors, the most likely power spectra for each CDM family are very consistent, especially at intermediate scales (30 – $50 h^{-1} \text{ Mpc}$), where the data information content provides the strongest constraint. Also shown in Fig. 4 are the best-fitting PS, obtained from similar likelihood analyses of the Mark III and SFI data sets. As can be seen, the most likely PS for the three catalogues are in good agreement. This result shows that the high-amplitude PS found from peculiar velocity data is unlikely to be due to possible non-uniformities of these catalogues or to the type of galaxies used. In fact, while Mark III and SFI relied predominantly on TF distances to spirals, ENEAR relies on D_n - σ distances to early-type galaxies. On the other hand, the reason for the discrepancy in the cosmological constraints between the maximum likelihood method and other methods (da Costa et al. 1998; Strauss & Willick 1995; Borgani et al. 2000a,b) remains unresolved. The former yields a systematically higher amplitude PS, as reflected by the high values of η_8 , which also disagrees with the constraints derived from other analyses of LSS data. Possible explanations are given in Section 5.

In all the COBE-normalized PS models considered the $\chi^2/\text{d.o.f.}$

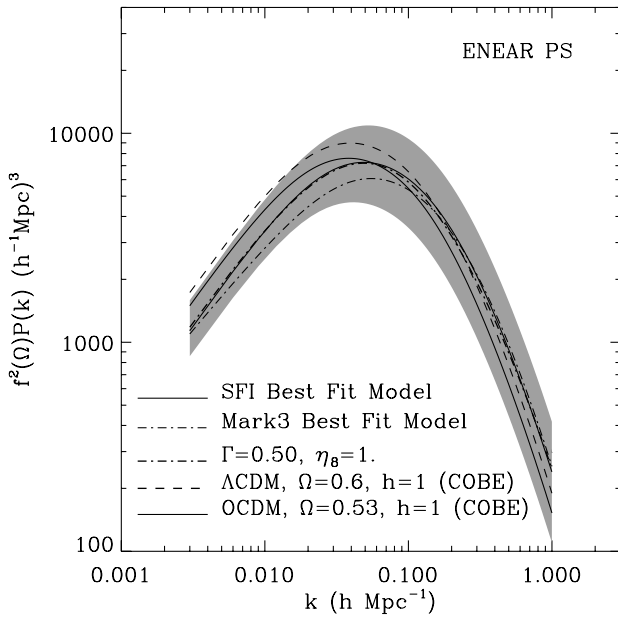


Figure 4. The PS of the most probable *COBE*-normalized OCDM (solid bold) and Λ CDM (dashed bold) models and of the Γ -model (dot-dashed bold). Also shown are the most probable models as estimated from Mark III (dot-dashed) and SFI (triple-dot-dashed) data sets. The shaded region around the PS marks the 3σ c.l. Note that the dynamical range of the data is confined to $0.05 \leq k \leq 0.3$.

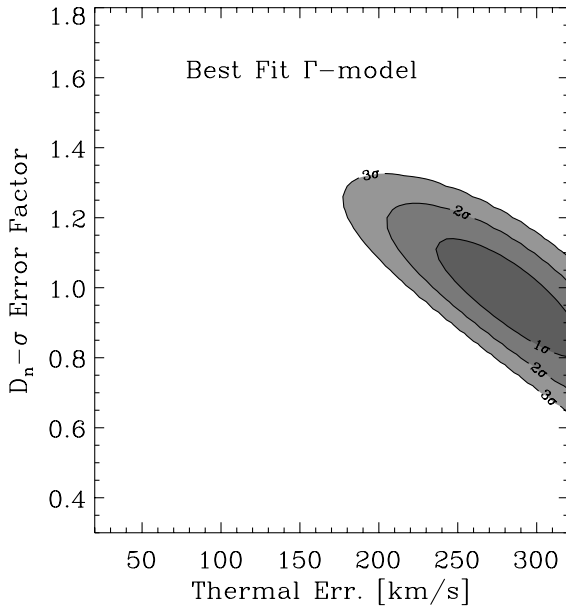


Figure 5. Contour map of \ln likelihood in the plane where the free parameters are the thermal error and a constant multiplicative factor for the D_n - σ error estimate. This calculation is performed assuming a cosmological model with $\eta_8 = 1$ and $\Gamma = 0.5$.

of the best-fitting models is of the order of 0.93. This value deviates by about 2σ from the $\chi^2/\text{d.o.f.}$ desired value of unity. However, this does not pose any serious problem because many of the models within the likelihood most likely contours have a $\chi^2/\text{d.o.f.} \approx 1$. The $\chi^2/\text{d.o.f.}$ for the Γ -model is 0.99.

3.4 Robustness of the results

In the present analysis there are a number of simplifying

assumptions which may give rise to systematic biases. In this subsection we address two possible sources of such biases, namely the adopted error model and the homogeneity of the data set.

In order to test the validity of our original error estimates we follow Freudling et al. (1999) and carry out the likelihood analysis with two additional free parameters to generalize the error model. The first is a constant multiplicative factor in front of the D_n - σ error and the second is the thermal component which is now allowed to be free. The analysis assumes that the PS is given by the best-fitting model previously obtained. The result of this analysis is presented in Fig. 5 which shows that the parameters originally used to describe the error model are within 1σ of the most likely values. Even though adding additional free parameters leads to larger formal errors, this result adds to our overall confidence in the original fit.

The homogeneity of the data set is addressed by running the likelihood analysis, with the original constant error estimates, for various cuts on the data. Adopting the best-fitting Γ -model obtained earlier, we carried out the likelihood analysis for the following subsets separately: northern hemisphere, southern hemisphere, distant galaxies ($>40 h^{-1}$ Mpc), nearby galaxies ($\leq 40 h^{-1}$ Mpc), cluster/group galaxies and ‘field’ galaxies – those are galaxies that have not been grouped with any other galaxy by our grouping algorithm. In all of these tests we obtain likelihood contours that are wider than those obtained from the full data set with some minor shifts in the most likely result. Nowhere in these tests do we get results that are inconsistent (at the 1σ level) with the original results. All runs yield the common feature of a high value for η_8 (≈ 1) and a very weak constraint on the value of Γ .

4 WIENER FILTER AND CONSTRAINED REALIZATIONS

4.1 The method

Having determined the power spectrum, all the ingredients needed to Wiener reconstruct the density and velocity fields are ready. Details on the general application of the WF/CR method to the reconstruction of large-scale structure are described in Zaroubi et al. (1995), where the theoretical foundation is discussed in relation to other methods of estimation, such as maximum entropy. The specific application of the WF/CR method to peculiar velocity data sets has been presented in Zaroubi et al. (1999). Here we provide only a brief description of the WF/CR method, for more details the reader is referred to the original references given above.

We assume that the peculiar velocity field is $\mathbf{v}(\mathbf{r})$ and the density fluctuation field $\delta(\mathbf{r})$ are related via linear gravitational-instability theory. Under the assumption of a specific theoretical prior for the power spectrum $P(k)$ of the underlying density field, one can write the WF minimum-variance estimator of the fields as

$$\mathbf{v}^{\text{WF}}(\mathbf{r}) = \langle \mathbf{v}(\mathbf{r}) u_i^o \rangle \langle u_i^o u_j^o \rangle^{-1} u_j^o \quad (11)$$

and

$$\delta^{\text{WF}}(\mathbf{r}) = \langle \delta(\mathbf{r}) u_i^o \rangle \langle u_i^o u_j^o \rangle^{-1} u_j^o. \quad (12)$$

A well known problem of the WF is that it attenuates the estimator to zero in regions where the noise dominates. The reconstructed mean field is thus statistically inhomogeneous. In order to recover statistical homogeneity we produce constrained realizations (CR), in which random realizations of the residual from the mean are generated such that they are statistically

consistent both with the data and the *prior* model (Hoffman & Ribak 1991; see also Bertschinger 1987). In regions dominated by good quality data, the CRs are dominated by the data, while in the limit of no data the realizations are practically unconstrained.

The CR method is based on creating random realizations, $\tilde{\delta}(\mathbf{r})$ and $\tilde{\mathbf{v}}(\mathbf{r})$, of the underlying fields that obey the assumed PS and linear theory, and a proper set of random errors $\tilde{\epsilon}_i$. The velocity random realization is then ‘observed’ like the actual data to yield a mock velocity data set \tilde{u}_i^o . Constrained realizations of the dynamical fields are then obtained by

$$\mathbf{v}^{\text{CR}}(\mathbf{r}) = \tilde{\mathbf{v}}(\mathbf{r}) + \langle \mathbf{v}(\mathbf{r}) u_i^o \rangle \langle u_i^o u_j^o \rangle^{-1} (u_j^o - \tilde{u}_j^o) \quad (13)$$

and

$$\delta^{\text{CR}}(\mathbf{r}) = \tilde{\delta}(\mathbf{r}) + \langle \delta(\mathbf{r}) u_i^o \rangle \langle u_i^o u_j^o \rangle^{-1} (u_j^o - \tilde{u}_j^o). \quad (14)$$

The two types of covariance matrices in the above equations are computed within the framework of linear theory as follows. The covariance matrix of the data $\langle u_i^o u_j^o \rangle$ is the same matrix \tilde{U}_{ij} that appears in equation (6).

The cross-correlation matrix of the data and the underlying field enters the above equations as, e.g.,

$$\langle \delta(\mathbf{r}) u_j^o \rangle = \langle \delta(\mathbf{r}) \mathbf{v}(\mathbf{r}_j) \rangle \cdot \hat{\mathbf{r}}_j. \quad (15)$$

The two-point cross-correlation vector between the density and velocity fields is related to the PS via

$$\langle \delta(\mathbf{x}) \mathbf{v}(\mathbf{x} + \mathbf{r}) \rangle = -\frac{H_0 f(\Omega_0)}{2\pi^2} \hat{\mathbf{r}} \int_0^\infty k P(k) j_1(kr) dk. \quad (16)$$

The assumption that linear theory is valid on all scales enables us to choose the resolution as well, and in particular to use different smoothing radii for the data and for the recovered fields. In our case no smoothing was applied to the radial velocity data, while we choose to reconstruct the density field with a finite Gaussian smoothing of radius R . This alters the density–velocity correlation function by inserting the multiplicative term $\exp[-k^2 R^2/2]$ into the integrand of equation (16).

A theoretical estimate of the signal-to-noise ratio (S/N) of the reconstructed fields at every point in space is given by a simple expression (see Zaroubi et al. 1999) but it requires the calculation and inversion of very large matrices. Therefore, in this study we estimate the point to point error by conducting a large number of CRs. In the case of random Gaussian fields, the ensemble of CRs defined in equations (13) and (14) samples the distribution of uncertainties in the mean Wiener density and velocity fields (Hoffman & Ribak 1991).

It is worth noting that the WF represents a general minimum-variance solution under the sole assumption that the field is a random field with a known power spectrum. No assumption has to be made here regarding higher order correlations (or the full joint probability distribution functions) of the underlying field. On the other hand, the CRs are derived under the explicit assumption of a full Gaussian random field.

4.2 Maps of density and velocity fields

Fig. 6 shows the map of the density field along the Supergalactic plane obtained from the ENEAR data using a Gaussian smoothing radius of 1200 km s^{-1} (hereafter G12). The shaded area corresponds to the region where the error, as estimated from performing 10 CRs, in density is less than 0.3. The main features of our local Universe are easily identified in the WF map, including

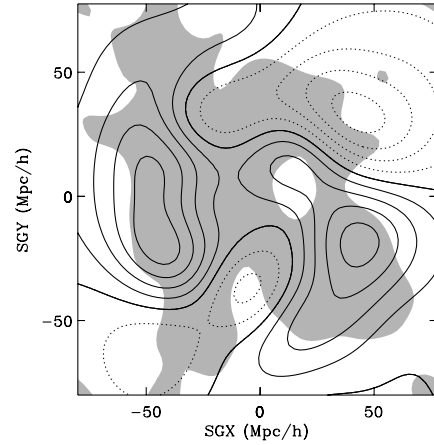


Figure 6. Density field reconstruction from the ENEAR catalogue in the Supergalactic plane, with G12 smoothing. Density contour spacing is 0.1, positive contours are solid, negative contours are dashed and $\delta = 0$ is denoted by the heavy solid line. The shading indicates regions where the error is less than 0.3.

the Great Attractor (GA) on the left and the Perseus–Pisces supercluster (PP) in the lower right. There is also a hint of the Coma cluster, which lies just outside the sample, in the upper part on the map. Even though different in detail, the gross features of the density field are remarkably similar to those obtained by Zaroubi, Hoffman & Dekel (1999) from the application of the same formalism to the Mark III catalogue. This is an outstanding result considering the different ways the two catalogues were constructed and the peculiar velocities measured.

The two upper panels in Fig. 7 compares a higher resolution map of the density field recovered from the ENEAR data (left panel) with the density field reconstructed from the PSCz redshift catalogue (right panel; Branchini et al. 1999). Both maps are along the Supergalactic plane and were reconstructed using a 900 km s^{-1} smoothing radius. The shaded area in the left panel indicates regions where the error is less than 0.45. Even though different in detail, the similarities between the density fields are striking and lend further credence to the reality of the structures observed in the mass distribution. Note that with the higher resolution some structures become resolved. For instance, one can clearly see the Local supercluster at the centre of the map. However, the apparent substructures that emerge in the GA and PP areas may not be real, owing to the lack of data within the Zone of Avoidance. The two lower panels of Fig. 7 show the overdensities within two additional planes parallel to the Supergalactic plane, at $Z = -25$ and $20 h^{-1} \text{ Mpc}$.

The velocity field (shown as streamlines) along the Supergalactic plane is presented in Fig. 8, showing the existence of two convergence regions which roughly coincide with the locations of the GA and PP.

4.3 Bulk velocity

The velocity field has been fitted using a monopole, dipole (i.e. bulk flow) and quadrupole (i.e. shear) expansion within spheres of radii ranging from 1000 to 6000 km s^{-1} – all volume-weighted. The three Cartesian components of the bulk velocity (in Supergalactic coordinates) and its absolute value (V_B) are shown in Fig. 9 as a function of the depth over which the fit has been done. The plots present the bulk velocity of the WF field and of an ensemble of 10 CRs. The plot of the absolute value of the bulk

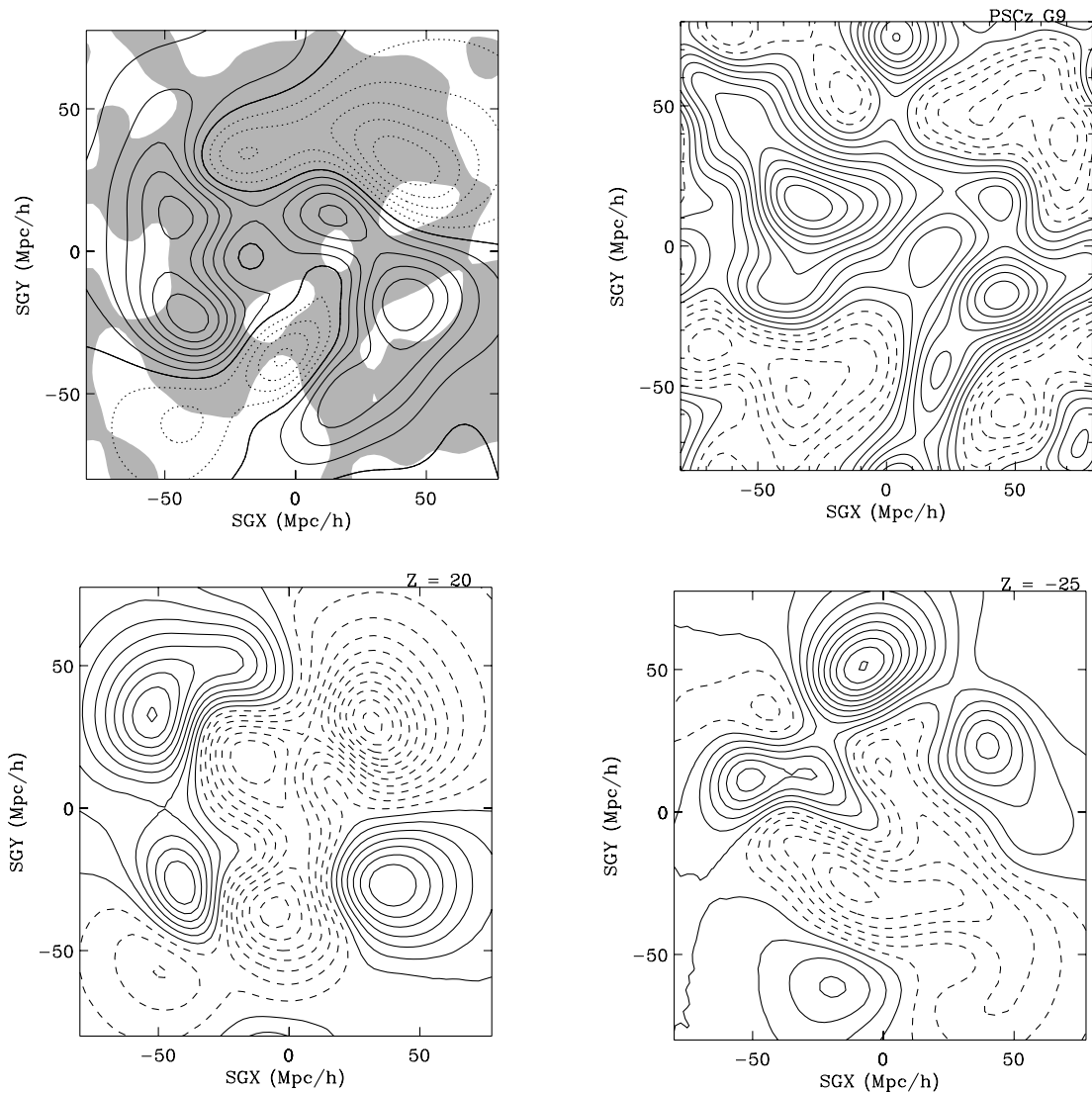


Figure 7. Upper left panel: the same as in Fig. 6 but with G9 smoothing. The shaded area indicates regions with an error smaller than 0.45. Upper right panel: the G9 smoothing density reconstruction from the PSCz redshift catalogue (Branchini et al. 1999). Lower left panel: the same as the upper left panel but for a plane parallel to the Supergalactic plane at $Z = +20 h^{-1}$ Mpc. Lower right panel: the same as the upper left panel but for a plane parallel to the Supergalactic plane at $Z = -25 h^{-1}$ Mpc.

velocity contains also the mean and standard deviation calculated over the ensemble of the CRs. Note that the mean V_B of the CRs is higher than its WF value because of the effect of error biasing (Lauer & Postman 1994). This result is expected as the WF attenuates the velocity field with the depth, as the observational errors become more dominant.

The amplitude of the bulk flow measured from the reconstructed three-dimensional velocity field ranges from $V_B = 300 \pm 70 \text{ km s}^{-1}$ for a sphere of $R = 20 h^{-1} \text{ Mpc}$ to $160 \pm 60 \text{ km s}^{-1}$ for $R = 60 h^{-1} \text{ Mpc}$. This value is in good agreement with that obtained from a direct fit to the radial peculiar velocities (da Costa et al. 2000b). This result disagrees with the bulk flow determined for the Mark III survey, which has an amplitude of roughly twice that of ENEAR (Zaroubi et al. 1999), but it is comparable to the one measured for the SFI sample. Table 1 shows the amplitude and direction the bulk flow in galactic coordinates within spheres of radii up to $60 h^{-1} \text{ Mpc}$. The errors in the table are estimated from the CRs ensemble.

4.4 Large-scale tidal field

An alternative description of the velocity field is to decompose it into two components, one which is induced by the local mass distribution and a tidal component resulting from mass fluctuations external to the volume considered. Here we follow the procedure suggested by Hoffman (1998a,b) and more recently by Hoffman et al. (2001). The key idea is to solve for the particular solution of the Poisson equation with respect to the WF density field within a given region and zero padding outside. This yields the velocity field induced locally, which hereafter we call the ‘divergent field’. The tidal field is then obtained by subtracting the divergent field from the full velocity field. Fig. 10 shows the results of this decomposition applied to the ENEAR survey, where the local volume is a sphere of $80 h^{-1} \text{ Mpc}$ centred on the Local Group. The plots show the full velocity field (upper left panel), the divergent (upper right panel) and the tidal (lower left panel) components. To understand the nature of the tidal field further its bulk velocity

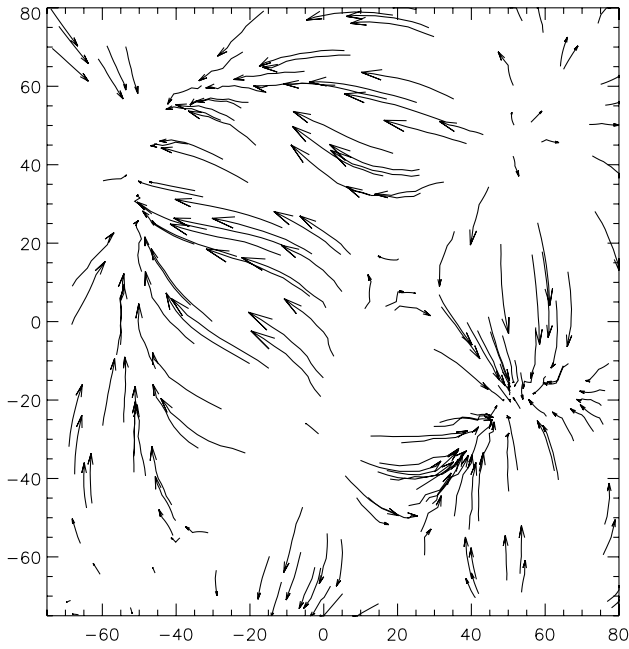


Figure 8. The G12 reconstructed velocity field in the Supergalactic plane is displayed as flow lines that start at random points, continue tangent to the local velocity field, and are of length proportional to the magnitude of the velocity at the starting point.

component has been subtracted and the residual is shown in the lower right panel. This residual is clearly dominated by a quadrupole component. In principle, the analysis of this residual field can shed light on the exterior mass distribution.

For the ENEAR catalogue we find that the local dynamics is hardly affected by structure on scales larger than its depth. For this sample both the bulk velocity at large radii and the rms value of the tidal field (estimated to be of the order of 60 km s^{-1}) are small. This is in marked contrast to the results obtained from the analysis of the Mark III survey which yields a much stronger tidal field, pointing (in the sense of its quadrupole moment) towards the Shapley concentration. For Mark III the tidal field contributes $\sim 200 \text{ km s}^{-1}$ to the total bulk velocity.

Table 1. Dipole component of the velocity field.

Radius $h^{-1} \text{ Mpc}$	$ \omega_p $ (km s^{-1})	l (degree)	b (degree)
10	443 ± 100	287 ± 26	71 ± 16
20	345 ± 73	306 ± 23	69 ± 13
30	236 ± 61	330 ± 21	61 ± 9
40	165 ± 58	344 ± 22	52 ± 8
50	117 ± 56	346 ± 25	47 ± 9
60	81 ± 57	330 ± 28	49 ± 15

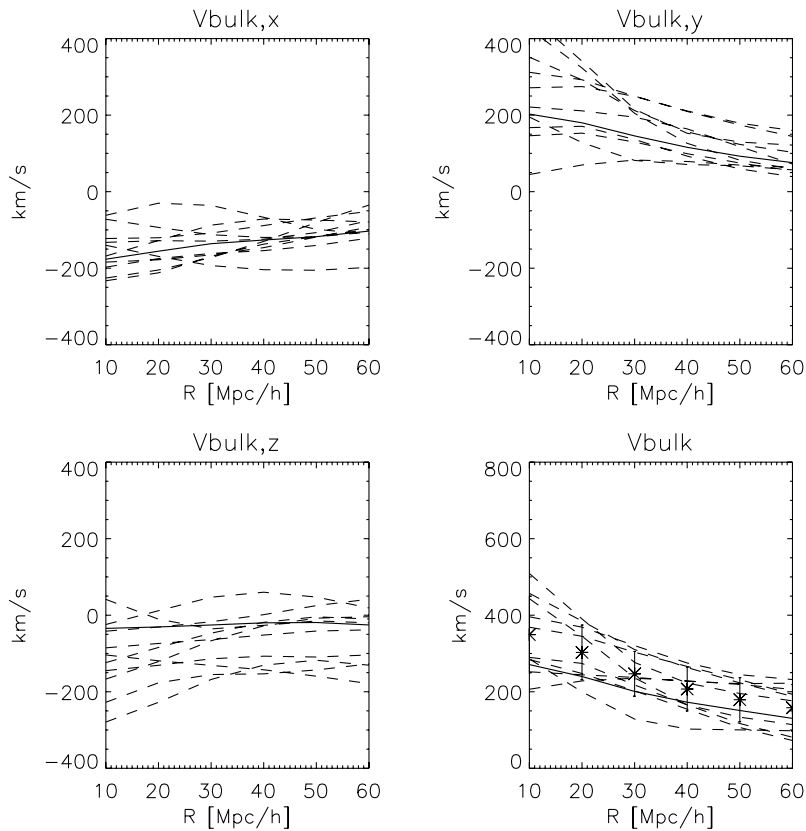


Figure 9. The bulk velocity fit of the reconstructed velocity field as a function of depth. The solid line corresponds to the WF field and the dashed lines correspond to an ensemble of 10 CRs. The four panels show the (Supergalactic) x , y and z components and the amplitude of the bulk velocity. The bottom right panel also presents the mean amplitude taken over the CRs and the error bars are the standard deviation around it. Note that this mean value is expected to be larger than the amplitude of the WF bulk velocity owing to the error bias effect (Lauer & Postman 1994).

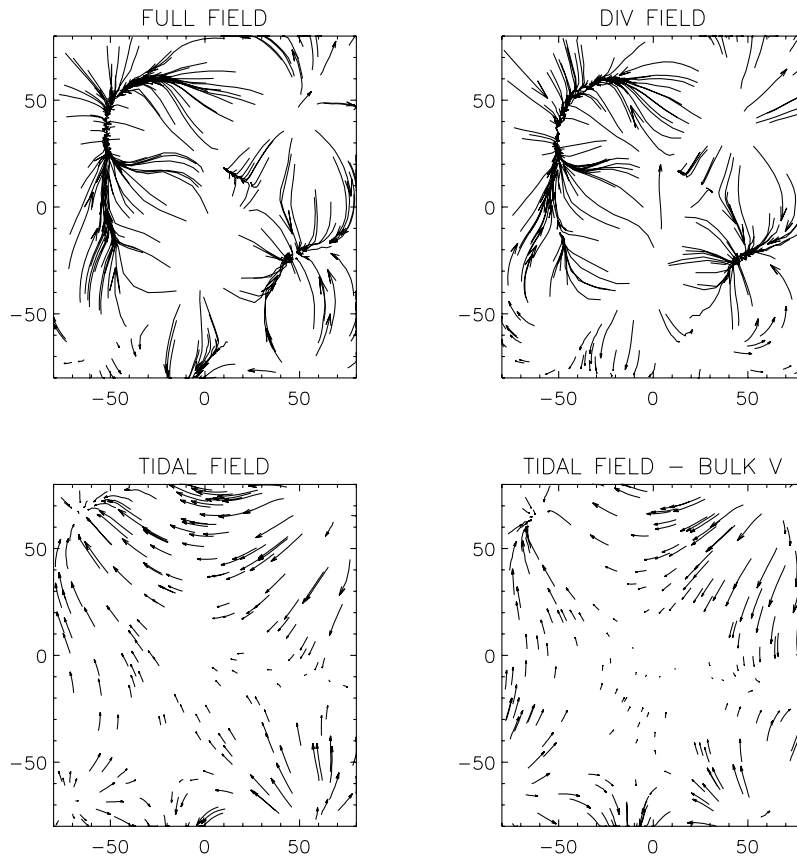


Figure 10. Tidal field decomposition of the G5 reconstructed velocity field in the Supergalactic plane is displayed as flow lines. The top left panel shows the full velocity field.

5 CONCLUSION

In the first part of this paper the maximum-likelihood method (Zaroubi et al. 1997) has been used to measure the mass–density power spectrum from the newly completed ENEAR early-type redshift–distance survey. The method assumes that the galaxy peculiar velocities satisfy Gaussian random statistics and that they are linearly related to the mass–density field. The initial fluctuation power spectrum is assumed to be CDM-like, with or without *COBE* normalizations. In addition the measured peculiar velocities error are assumed to be proportional to the distance with some thermal component to account for the non-linear evolution of high-density environment in which the early-type galaxies reside.

General results valid for all the models used in the analysis, independent of the detailed parametrization and normalization of each model, can be summarized as follows. The amplitude of the power spectrum at $k = 0.1 h \text{ Mpc}^{-1}$ is $P(k)\Omega^{1.2} = (6.5 \pm 3) \times 10^3 (h \text{ Mpc}^{-1})^3$ yielding $\eta_8 = 1.1^{+0.2}_{-0.35}$. For the family of *COBE*-normalized CDM models the following range of parameters was considered: $\Omega \leq 1$; $0.4 < h < 1$; and $n = 1$. Within this range we have obtained a constraint on a combination of the parameters Ω and h which can be approximated by $\Omega \approx (0.38 \pm 0.08) h^{-1.3}$ for Λ CDM, and $\Omega \approx (0.52 \pm 0.083) h^{-0.88}$ for OCDM. For $h = 0.65$, Λ CDM yields $\Omega = 0.5\text{--}0.8$. Similar constraints are obtained from the analysis of the generic Γ -models, independent of the *COBE* normalization. We find that the power spectrum amplitude and shape parameter are constrained to be $\eta_8 = 1.0^{+0.3}_{-0.28}$ and $\Gamma \geq 0.18$, with larger values of Γ (>0.4) being more probable. We point out that these constraints are consistent with the results

obtained from a similar analysis of the Mark III and the SFI peculiar velocity catalogues. This agreement is encouraging because it shows that the results are robust and independent of the sample used.

Examination of the $\chi^2/\text{d.o.f.}$ for the most likely *COBE*-normalized models shows that their values are of the order of 0.93. These values are about 2σ away from the preferred value of 1. However, this should not be too alarming as many of the models within the errors have $\chi^2/\text{d.o.f.} \sim 1$. The $\chi^2/\text{d.o.f.}$ for the best-fitting Γ -model is 0.99.

As pointed out by previous papers that have analysed the PS derived from peculiar velocity data (Zaroubi et al. 1997; Freudling et al. 1999), the constraints on η_8 and Γ are considerably higher than those obtained from other types of analyses including peculiar velocity data (Borgani et al. 1997, 2000a,b), cluster abundances and the galaxy power spectrum (Efstathiou et al. 1992; Sutherland et al. 1999). They are also inconsistent with those obtained by combining the results from high-redshift supernovae type Ia (Perlmutter et al. 1999) and the CMB data (Efstathiou et al. 1999), which yield values of $\Omega \approx 0.25 \pm 0.15$ and $\Lambda \approx 0.65 \pm 0.2$. Furthermore, assuming a linear galaxy–mass relation the value of η_8 obtained from the present analysis would imply a $\beta_I \sim 1.4$, where the subscript refers to *IRAS* galaxies, at least a factor of 2 larger than those derived from a velocity–velocity comparison of the *IRAS* 1.2-Jy gravity field and the Mark III (Davis et al. 1996), SFI (da Costa et al. 1998) and ENEAR (Nusser et al. 2001), all leading to $\beta_I \sim 0.5$.

It is important to point out that the method is very sensitive to the assumed error model, which can add or suppress power. It also

implicitly gives a high weight to nearby galaxies, likely to be slow rotators or low-velocity dispersion systems, for which the measurements and the distance relations are the least reliable. However, tests show that these effects are unimportant for the present data set. Another potential problem arises because of the rapid decrease of the weight with distance: the effective volume of the currently available catalogues is small and the shape of the power spectrum is poorly constrained, as illustrated by the case of the Γ -model. All these factors may impact on the reliability of the constraints obtained from the PS analysis.

Finally, one or more of the theoretical model ingredients could be inaccurate, e.g. power spectrum assumed shapes, Gaussianity of the distribution, or even some inherent bias in the method itself that has eluded the extensive numerical tests carried out with the data and mock samples (e.g. Freudling et al. 1999). In fact, Hoffman & Zaroubi (2000) have recently suggested a theoretical framework for analysing the consistency of the most probable model with the data. The approach is based on an eigenmode expansion of the data covariance matrix and then a performance of a goodness-of-fit analysis on a mode-by-mode basis. Hoffman & Zaroubi applied the test to the MARK III and the SFI catalogues and found a systematic inconsistency of the data with their ‘best-fitting’ models. A similar result has been found also for the ENEAR data (to be published elsewhere). This points to a generic problem with the theoretical framework used to analyse the data that is common to (at least these three) velocity surveys. Possible sources of this problem might lie with non-linear dynamical effects, incorrect treatment of (systematic and statistical) errors or the assumption of the wrong power spectrum. Further experimentation with the data and models should be done before this inconsistency can be resolved.

Finally, in this study we have also performed, given the most probable power spectrum, a Wiener reconstruction of the density and velocity fields. The maps shown here have 1200 km s^{-1} and 900 km s^{-1} Gaussian resolution and they are limited to the Supergalactic plane. The main features shown are similar to the features in the *IRAS* reconstruction, corrected for peculiar velocities. The constrained realizations allow us to estimate the point-by-point uncertainties in the recovered maps. In terms of their recovered density fields ENEAR, SFI and Mark III mostly agree. However, they do differ in the velocity fields. ENEAR shows no significant tidal component while it contributes significantly to the Mark III bulk velocity. This tidal field accounts for the very different bulk velocities obtained from ENEAR and Mark III, with SFI situated between these surveys. The results suggest that volumes of $60\text{--}80 h^{-1} \text{ Mpc}$ are essentially at rest relative to the CMB and that the Local Group motion is primarily caused by mass fluctuations within the volume sampled by the existing catalogues of peculiar velocity data.

ACKNOWLEDGMENTS

We thank Enzo Branchini for providing the PSCz density field. We would also like to thank the referee M. Strauss for his careful reading of the paper and numerous suggestions for its improvement. We acknowledge Avishai Dekel, Enzo Branchini, Tony Banday, Ravi Sheth, Simon White and Idit Zehavi for stimulating discussions. SZ gratefully acknowledges the hospitality of Kapteyn Astronomical Institute – Groningen. The authors thank M. Maia, C. Rit  and O. Chaves for their contribution over the years. MB thanks the Sternwarte M nchen, the Technische Universit t M nchen, ESO Studentship program, and MPA Garching for their financial support during different phases of this research.

MVA is partially supported by CONICET, SecyT and the Antorchas–Andes–Vitae cooperation. GW is grateful to the Alexander von Humboldt-Stiftung for making possible a year’s stay at the Ruhr-Universit t in Bochum, and to ESO for support for visits to Garching which greatly aided this project. Financial support for this work has been given through Israel Science Foundation grant 103/98 (YH); Binational Science Foundation grant 94-00185 (YH), FAPERJ (CNAW, MAGM, PSSP), CNPq grants 201036/90.8, 301364/86-9 (CNAW), 301366/86-1 (MAGM); NSF AST 9529098 (CNAW); ESO Visitor grant (CNAW). PSP and MAGM thank CLAF for financial support and CNPq fellowships. The results of this paper are based on observations at Complejo Astronómico El Leoncito (CASLEO), operated under agreement between the Consejo Nacional de Investigaciones Científicas de la República Argentina and the National Universities of La Plata, Córdoba and San Juan; Cerro Tololo Interamerican Observatory (CTIO), operated by the National Optical Astronomical Observatories, under AURA; European Southern Observatory (ESO), partially under the ESO-ON agreement; Fred Lawrence Whipple Observatory (FLWO); Observat rio do Pico dos Dias, operated by the Laborat rio Nacional de Astrof sica (LNA); and the MDM Observatory at Kitt Peak.

REFERENCES

- Bennett C. L. et al., 1996, *ApJ*, 464, L1
 Bertschinger E., 1987, *ApJ*, 323, L103
 Borgani S., da Costa L. N., Freudling W., Giovanelli R., Haynes M. P., Salzer J., Wegner G., 1997, *ApJ*, 482, L121
 Borgani S., Bernardi M., da Costa L. N., Wegner G., Alonso M. V., Willmer C. N. A., Pellegrini P. S., Maia M. A. G., 2000a, *ApJ*, 537, L1
 Borgani S., da Costa L. N., Zehavi I., Giovanelli R., Haynes M., Freudling W., Wegner G., Salzer J. J., 2000b, *AJ*, 119, 102
 Branchini E. et al., 1999, *MNRAS*, 308, 1
 Bunn E. F., Fisher K. B., Hoffman Y., Lahav O., Silk J., Zaroubi S., 1994, *ApJ*, 432, L75
 Burles S., Tytler D., 1998, *ApJ*, 507, 732
 da Costa L. N., Freudling W., Wegner G., Giovanelli R., Haynes M. P., Salzer J. J., 1996, *ApJ*, 468, L5
 da Costa L. N., Nusser A., Freudling W., Giovanelli R., Haynes M. P., Salzer J. J., Wegner G., 1998, *MNRAS*, 299, 425
 da Costa L. N., Bernardi M., Alonso M. V., Wegner G., Willmer C. N. A., Pellegrini P. S., Maia M. A. G., Zaroubi S., 2000a, *ApJ*, 537, L81 (Paper I)
 da Costa L. N., Bernardi M., Alonso M. V., Wegner G., Willmer C. N. A., Pellegrini P. S., Rit  C., Maia M. A. G., 2000b, *AJ*, 120, 95
 Davis M., Nusser A., Willick J. A., 1996, *ApJ*, 473, 22
 Efstathiou G., Bond J. R., White S. D. M., 1992, *MNRAS*, 258, 1P
 Efstathiou G., Bridle S. L., Lasenby A. N., Hobson M. P., Ellis R. S., 1999, *MNRAS*, 330, L47
 Fisher K. B., Lahav O., Hoffman Y., Lynden-Bell D., Zaroubi S., 1995, *MNRAS*, 272, 885
 Freudling W. et al., 1999, *ApJ*, 523, 1
 Geller M. J., Huchra J. P., 1983, *ApJS*, 52, 61
 G rski K. M., 1988, *ApJ*, 332, L7
 Groth E. J., Juszkiewicz R., Ostriker J. P., 1989, *ApJ*, 346, 558
 Hoffman Y., 1998a, in Colombi S., Mellier Y., Raban B., eds, *Wide Field Surveys in Cosmology*. Editions Frontieres, Paris, p. 105
 Hoffman Y., 1998b, in Banday A. J., Sheth R. K., da Costa L. N., eds, *Proc. Evolution of Large Scale Structure-Garching*. PrintPartners Ipskamp, Enschede, p. 148
 Hoffman Y., Ribak E., 1991, *ApJ*, 380, L5
 Hoffman Y., Zaroubi S., 2000, *ApJ*, 535, L5

- Hoffman Y., Eldar A., Zaroubi S., Dekel A., 2001, *ApJ*, submitted (astro-ph/0102190)
- Haynes M. P., Giovanelli R., Chamaraux P., da Costa L. N., Freudling W., Salzer J. J., Wegner G., 1999a, *AJ*, 117, 2039
- Haynes M. P., Giovanelli R., Salzer J. J., Wegner G., Freudling W., da Costa L. N., Herter T., Vogt N. P., 1999b, *AJ*, 117, 1668
- Jaffe A. H., Kaiser N., 1995, *ApJ*, 455, 26
- Kaiser N., 1987, *MNRAS*, 227, 1
- Kaiser N., Stebbins A., 1991, in Latham D. W., da Costa L. N., eds, *ASP Conf. Ser. Vol. 15, Large Scale Structure and Peculiar Motions in the Universe*. Astron. Soc. Pac., San Francisco, p. 111
- Lahav O., Fisher K. B., Hoffman Y., Scharf C. A., Zaroubi S., 1994, *ApJ*, 423, L93
- Lauer T. R., Postman M., 1994, *ApJ*, 425, 418
- Lynden-Bell D., Faber S. M., Burstein D., Davies R. L., Dressler A., Terlevich R., Wegner G., 1988, *ApJ*, 326, 19
- Maia M. A. G., da Costa L. N., Latham D. W., 1989, *ApJS*, 69, 809
- Nusser A., da Costa L. N., Branchini E., Bernardi M., Alonso M. V., Wegner G., Willmer C. N. A., Pellegrini P. S., 2001, *MNRAS*, 320, L21
- Perlmutter S. et al., 1999, *ApJ*, 517, 565
- Press W. H., Teukolsky S. A., Vetterling W. T., Flannery B. P., 1992, *Numerical Recipes*. Second edn. Cambridge Univ. Press, Cambridge
- Ramella M., Pisani A., Geller M. J., 1997, *AJ*, 113, 483
- Strauss M. A., Willick J. A., 1995, *Phys. Rep.*, 261, 271
- Sugiyama N., 1995, *ApJS*, 100, 281
- Sutherland W. et al., 1999, *MNRAS*, 308, 289
- Wiener N., 1949, *Extrapolation and Smoothing of Stationary Time Series*. Wiley, New York
- Willick J. A., Courteau S., Faber S. M., Burstein D., Dekel A., Strauss M. A., 1997, *ApJS*, 109, 333
- Zaroubi S., Hoffman Y., 1996, *ApJ*, 462, 25
- Zaroubi S., Hoffman Y., Fisher K. B., Lahav O., 1995, *ApJ*, 449, 446
- Zaroubi S., Zehavi I., Dekel A., Hoffman Y., Kolatt T., 1997, *ApJ*, 486, 21
- Zaroubi S., Hoffman Y., Dekel A., 1999, *ApJ*, 520, 413

This paper has been typeset from a $\text{\TeX}/\text{\LaTeX}$ file prepared by the author.